Phenomenology and Detectability of Quantum Effects in Gravitational Waves Emitted by Binary Black Hole Mergers

LIGO SURF 2020: Final Report

Zoë Haggard
Pomona College

Mentors: Alan J. Weinstein and Colm Talbot
LIGO Collaboration, Caltech

(Dated: October 5, 2020)

Gravitational waves detected by Advanced LIGO and Advanced Virgo provide a test of the theory of general relativity in the strong-field, highly dynamical regime, such as in compact binary coalescences. General relativity, a purely classical theory, does not incorporate quantum mechanics. It is thought, however, that quantum mechanics must modify gravity; quantum uncertainty must manifest itself during the merger of two black hole horizons. These quantum mechanical effects could be observable in gravitational waves detected by LIGO as small perturbations in the signal waveform and higher harmonics, not explainable by current understandings of general relativity. We study both the *phenomenology* and *detectability* of such quantum mechanical effects from binary black hole mergers for future LIGO observations.

I. MOTIVATION

In his general theory of relativity (GR), Einstein predicts the existence of gravitational waves. Just as an accelerating charge produces electromagnetic radiation, an accelerating mass will create gravitational radiation, or, gravitational waves (GWs). GWs emit outwards at the speed of light. In the far-field, GWs are described by a strain with two polarizations (h_+ and $h_\times$), which can be combined into a complex waveform, $h = h_+ - ih_\times$. The passing waves cause the distance between freely falling objects ('test masses') to oscillate at the frequency and amplitude of the GWs [1]. But gravitation, compared to electromagnetism, is much weaker. To observe gravitational radiation on Earth, highly massive and dynamic systems – such as coalescing compact binary black hole (BBH) systems – are needed in conjunction with large and precise detectors. In recent years, the Laser Interferometer Gravitational-Wave Observatory (LIGO) and Advanced Virgo have successfully observed GWs from compact binary mergers [2, 3].

The coalescence of a BBH system is defined by three major phases: inspiral, merger, and ringdown [4]. In the inspiral, the two black holes emit gravitational waves (roughly) twice the orbital frequency of the binary source; their orbital radius decreases with the GW emission. After the last stable orbit, the two horizons plunge into each other and merge during the merger phase. Finally, once the BHs' horizons come together, the merged, remnant BH falls to equilibrium in the ringdown by emitting GWs at specific modes, called quasi-normal modes (QNMs). The frequency and damping time of these modes can be calculated from black hole perturbation theory, which takes into account the final black hole's spin and mass; amplitude and phase of the modes, however, depend on the characteristics of the merger [5].

Generally, the ringdown strain ($h = h_+ - ih_\times$) at a GW-detector is written as a linear superposition of damped sinusoids, each j term being a single QNM:

$$h(t) = \sum_{j=1} A_j e^{2i\pi f_{0,j} t + i\phi_j} e^{-\frac{t}{\tau_j}} \tag{1}$$

where A_j is the amplitude of term j, $f_{0,j}$ is the central frequency of the particular QNM, ϕ_j is the phase shift, and τ_j is the decay time, or the time required for the amplitude to drop by a factor of $1/e$ [6]. Again, the frequency of a mode ($f_{0,j}$) and the damping time (τ_j) are predicted solely from the mass of the system, while amplitude (A_j) and phase (ϕ_j) are dependent on *how* the black holes merged. As a note, $f_{0,1} = \Re(\omega_1)/(2\pi)$ and $1/\tau_j = \Im(\omega_j)$ where ω_j is the angular frequency of the j'th mode.

Calculating these modes is a challenge and many methods have be used to numerically (or semi-analytically) calculate the full spectrum of QNMs [7]. Because of the difficulty of creating waveforms with a full spectrum of QNM, early LIGO waveforms only utilized the (l=2, m=2) mode, or the quadrupole. This is not necessarily a bad assumption, as for quasi-circular binary mergers the loudest QNM tends to the quadrupole; higher modes have magnitudes that are much smaller than the dominant quadrupole, making them hard to disentangle from the noise. With just the (2, 2) mode, intrinsic characteristics, such as the individual BH's mass and spin, and extrinsic characteristics, such as location, inclination (relative to the observer's line of sight), and the time of merger, can be inferred from the strain received at a network of detectors [8]. For instance, notice how the the complex angular frequency of the quadrupole for a gravitationally perturbed Schwarzschild BH only depends on mass, M:

$$\omega_{(2,2,0)} = \frac{0.7474c}{R_s} - i\frac{0.178c}{R_s} \tag{2}$$

where c is the speed of light and R_s is the Schwarzschild radius, $2GM/c^2$ [5]. As an example, a BH with $10M_\odot$ will have a quadrupolar frequency $\Re(\omega)/2\pi$ of 1207 Hz and a damping time $1/\Im(\omega)$ of 0.55 ms.

The Fourier transform, which shifts to the frequency domain, is a useful tool for signal analysis and is employed in our study. The Fourier transform of a damped sinusoid is the Lorentzian [9]. Centered at f_0, the Lorentzian is written as,

$$\tilde{h}(f) = \sum_{j=1} A_j e^{i\phi_j} \frac{1}{2\pi} \frac{\gamma_j}{((f_j - f_{0,j})^2 + \frac{1}{2}{\gamma_j}^2)} \tag{3}$$

where $f_{o,j}$ is the frequency of the mode and $\gamma_j = \frac{1}{\tau_j}$.

Recently, however, with advances in waveforms that include more than the (2, 2) mode, higher harmonics have been observed in compact binary mergers. GW190412 and GW190814, for instance, both show evidence of an octopole (3, 3) mode [6, 10]. This opens up a new domain for testing more finely the predictions of GR, as every QNM is predicted by the theory. As of yet, there have been no inconsistencies found, but the study of higher order modes – black hole spectroscopy – presents a way to uncover deviations from GR.

Deviations from GR are expected, for instance, from quantum mechanical effects. There is no unified theory of gravity and quantum mechanics; GR and quantum mechanics, among other things, disagree about what happens past the event horizon of a BH. In the classical GR picture, the inside of a BH is empty except for the infinitely dense region of the singularity. But, according to quantum mechanics, quantum uncertainty should become important on Planck scales; meaning, near the singularity, space is not empty, but full of quantum fluctuations of matter fields [11].

One way to get around this conundrum is to explore what would happen if a black hole was in fact a BH-imitator, or an exotic compact object (ECO). ECOs, which are included in various theories of quantum gravity around BHs. An ECO is *not* empty, but is rather made up of some form of exotic matter. There, however, are very few concrete predictions of the observable differences these ECOs would produce.

Recent work done by Brustein *et al*, which incorporates a collapsed polymer model ECO, finds differences in the quasi-normal ringdown spectrum [11–13]. The collapsed polymer models the BH as a Schwarzschild-radius sized soup of interacting, closed strings. The polymer is elastic and when disturbed (as in a merger) dissipates energy by oscillation at a specific mode. We can find the mode of oscillation by treating the stringy matter as a fluid with an index of refraction, n_{ref}, where n_{ref} is defined as v_{sound}/c. Matching the boundary conditions between inside and outside the polymer, it is found that relativistic modes ($v_{sound} \lesssim c$) are suppressed, while subrelativistic modes ($v_{sound} << c$) are able to leak past the horizon. In other words, n_{ref} must be greater than 1 [13].

The index of refraction can also be related to the properties of the matter. In the stringy polymer case, n_{ref} inversely depends on the likelihood of string interaction, g_s, or the quantum string coupling; this a number between 0 and 1. In the GR limit, g_s is 0, implying zero interaction between stringy matter, and thus an infinite n_{ref}; in other words, no modes can leak past the horizon. A large g_s, on the other hand, implies many interactions between strings [14]. A g_s close to 1 is nonphysical, however, as an analysis of GW150914 and GW151226 suggest that g_s^2, using this model, is (roughly) less than 0.65 [13]. This translates to an n_{ref} of at *least* 1.25.

In summary, as the BH-imitator is deformed during the ringdown, and the stringy fluid creates additional fluid modes that are quantum in origin. These modes have specific complex angular frequencies in *addition* to the regular GR modes. In the limit of $n_{ref} > 1$ – subrelativistic modes – these angular frequencies can be written as,

$$\omega_p = \frac{pc\pi}{2R_s n_{ref}} - i\frac{c}{R_s n_{ref}^2} \tag{4}$$

where p is an odd integer, c is the speed of light, R_s is equivalent to the r_+ Kerr solution, and n_{ref} is the refractive index of the matter. In this work we focus on the non-spinning solution as Brustein *et al* are less certain about the modes in the solution where spin in non-zero. In the limit that $\chi = 0$, the Kerr reduces to the Schwarzschild. If we compare the $p = 1$ mode to the gravitationally perturbed Schwarzschild (2, 2) mode (Equation 2), given that n_{ref} must be greater than 1, we see that the fluid mode has a lower frequency (by around a factor of $1/n_{ref}$) and a longer damping time (by around a factor of $6n_{ref}^2$). The GR and polymer real frequencies are equivalent (i.e. indistinguishable) when $n_{ref} \sim 2$.

In the time domain, these additional ringdown modes have the same form as Equation 1, but are composed of different frequencies, amplitudes, and damping times [13]. We do not know when these modes begin relative to GR modes, so it's assumed that they begin sometime during the first cycle, or $t_s \sim 1/\Re\omega$.

The full ringdown, including both quantum and GR modes is, will look like,

$$h(t) = \sum_{j=1} A_j e^{2i\pi f_{0,j} t + i\phi_j} e^{-\frac{t}{\tau_j}} + \sum_{p=1} A_p e^{2i\pi f_{0,p} t_p + i\phi_p} e^{-\frac{t_p}{\tau_p}} \tag{5}$$

where each j term corresponds to a GR mode and each p term (where p is an *odd* integer) corresponds to a quantum mode. Here A_j is the amplitude of a GR mode, $f_{0,j}$ is the central frequency of the particular GR mode, ϕ_j is the phase shift of a GR mode, and τ_j is the decay time of a GR mode. Here A_p is the amplitude of a quantum mode, $f_{0,p}$ is the central frequency of the particular quantum mode, ϕ_p is the phase shift of a quantum mode, and τ_p is the decay time of a quantum mode. It is important to note that both $\delta\phi_p$ and A_p are not well predicted by the collapsed polymer model, and depend on *how* the

BBH system came together; for this reason, they will be treated as free parameters.

II. PROJECT & METHOD OVERVIEW

This project focuses on testing and employing the quantum modes described by Brustein *et al* [12, 13]. The main work of this project is to determine (1) the phenomenology of the quantum modes and (2) whether the quantum modes are *significantly* detectable by the LIGO network at various signal-to-noise ratios (SNRs), BH binary masses, and n_{ref}. The goal is to find an optimal mass range for detecting these new fluid modes.

First, *without* using the quantum mode, we explore classical GR predictions for the ringdown: what frequencies and damping times are predicted? Next, we simulate a noiseless signal and fit for ringdown modes, verifying that we can at least recover them without the GR mode. We recover the signal with `scipy.optimize` which uses least-squared fitting [15].

Next, we move on to the *phenomenology* of the quantum mode, exploring the frequency and damping times for various masses and n_{ref}. Here, the goal is to visually see how these new modes compare to GR modes. For our analysis, we set the dimensionless spin between $\chi = 0.1$ and $\chi = 0.7$. As a note, it is *not* known how the quantum modes depend on χ; this test is more to understand the phenomenology of the GR modes (which are known to depend on χ). In general, in the $\chi = 0$ case, based on equations 4 and 2 (for $p = 1$), the new quantum mode is expected to be (roughly) lower in frequency and longer lived than the dominant GR quadrupole mode.

Understanding the phenomenology of the mode, we explore the *detectability of a single quantum mode*. To do this, we characteristic detector noise to our quantum mode and experiment with signal-to-noise ratio (SNR) and its relation to BH mass for various values of n_{ref}. For this, our parameters are the quantum signal's amplitude (proxy for SNR), BH mass (in units $M_\odot$), and n_{ref}. We sample mass between $20M_\odot$ and $200M_\odot$, and work with n_{ref} between 3 and 10. We choose to work in this n_{ref} range because it is (1) above the value where the real frequency of the GR mode and quantum mode would overlap ($n_{ref} \approx 2$) and (2) prohibitively large n_{ref} will have very low frequencies, undetectable by LIGO and its partners (see Figure 1). We keep $\chi = 0$ and make a model of *just* the $p = 1$ quantum mode.

We perform our analysis in `bilby` (which works in the frequency domain) at high SNR or high amplitude signals [16, 17]. We set the start time of the quantum modes and start time of analysis to be at $t = 0$. Detection significance, or how well our model is able to match to our simulated signal, is measured by the Bayes factor, which is the likelihood ratio between the quantum model and the null hypothesis (noise). A large Bayes factor (greater than 100) is strong evidence for the quantum model. From this we should get an optimal mass range for detection for a given n_{ref} value. The optimal mass range *should* differ depending on n_{ref} value; this analysis gives us a mass value at which SNR peaks for a given n_{ref}, which we call the peak mass.

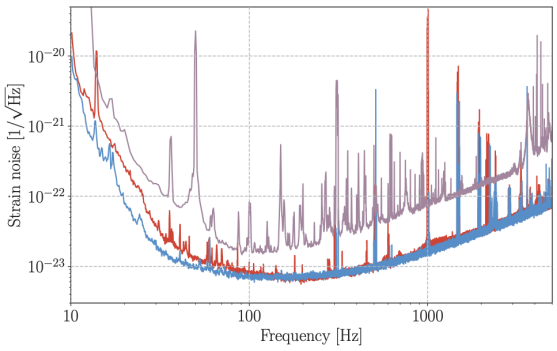

FIG. 1. Noise curves for L1 (blue), H1 (red), and Virgo (purple) [8]. Notice the least noisy band is on the order of 100 Hz.

Having explored the phenomenology and detectability of a sole quantum mode, we add the quantum mode to a *full ringdown* (with higher order modes) provided by NRSur7dq4 [18]. Our goal is to (1) see whether the mode can be recovered within a full ringdown and (2) see what parameters (n_{ref} and corresponding peak mass) result in the *best* recovery. In this analysis, because we have a superposition of NRSur7dq4 and the quantum mode – which we choose to start at $t_s \sim 1/\omega_{real}$, relative to the GR mode – we must make sure there is no discontinuity in the waveform caused by the addition. We add the quantum mode multiplied by a sigmoid function to NRSur7dq4 to smooth out any sharpness, and taper the waveform. The sigmoid-multiplied quantum waveform is as follows:

$$h(t)_{sig} = \frac{A_p}{1 + e^{-4096(t-2t_p)}} e^{2i\pi f_{0,p} t_p + i\phi_p} e^{-\frac{t_p}{\tau_p}} \quad (6)$$

Here, $h(t)_{sig}$ is the final sigmoid-multiplied strain in the time-domain. A_p is the amplitude of the quantum mode, t_p is the start time of the quantum mode, and $f_{0,p}$ is the frequency of the quantum mode. As an example, we show the effect of the sigmoid taper in Figure 2. We see that with the sigmoid (orange in Figure 2), the discontinuity caused by adding the quantum mode is smoothed out.

For our analysis, we sample recovery at various n_{ref} using the peak masses we found in the previous analysis. For our priors, in order to speed up analysis, we only sample damping time (τ_p) and frequency ($f_{0,p}$), and set the priors for all other parameters to be their true values (amplitude of the quantum mode, phase of the quantum mode, start time of the quantum mode, and NRSur7dq4 waveform parameters).

For each n_{ref}, we inject both loud signals (large amplitudes compared to the NRSur7dq4 waveform) and quiet signals (small amplitudes compared to the NRSur7dq4 waveform).

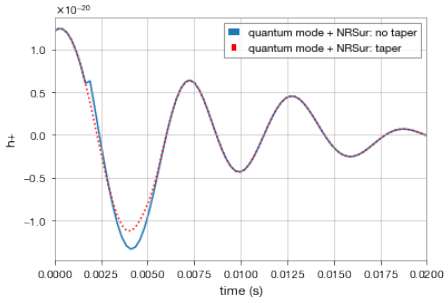

FIG. 2. Plot of h+ from $t = 0$ for NRSur7dq4+quantum mode untapered (blue) and NRSur7dq4+quantum mode tapered (red). Here, we used $n_{ref} = 3$ and $A_p = 6 \times 10^{-21}$ for the quantum mode, and set $M = 100M_\odot$, $\chi = 0$, and distance = 100 Mpc, inclination = 0, and q = 1. We see a small discontinuity around the point where the quantum mode is added ($t \approx 0.02$).

III. RESULTS

A. Recovery of GR modes

Using NRSur7dq4 and the `qnm` package, we study whether we could recover the expected QNM frequency for a single mode using a damped-sinusoid curve fit (with NRSur7dq4). We choose to work with the fundamental (2, 2) mode, with $M = 44$, $\chi = 0$, and $q = 1$. From the `qnm` package, this mode should have a frequency of 354 Hz and a decay time of 0.002 seconds. Using `scipy.optimize.curve_fit`, we find that the fit gives results within the order of the expected QNM: a frequency around 360 Hz and a decay time around 0.002 seconds (Figure 3). So, we can recover the mode as predicted by GR.

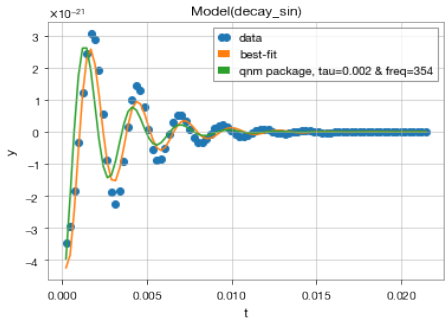

FIG. 3. Fit of NRSur7dq4 model for fundamental (2, 2) mode and $M = 44$, $\chi = 0$, $q = 1$, distance = 235 Mpc. Here, blue is the NRSur7dq4 model, orange is the resulting fit to a general damped sinusoid, and green is a plot of the damped sinusoid with ringdown parameters from `qnm`. The fit finds that $\tau = 0.002$ s and $f = 360$ Hz, while the `qnm` package finds that $f = 354$ Hz and $\tau = 0.002$ s.

B. Phenomenology of the Quantum mode

Since we do not know how the quantum mode depends on spin (χ) in Brustein *et al*'s model, our choice for n_{ref} and mass just influences the frequency and damping time of the quantum modes. Spin and mass influence the frequency and damping time of the classic GR mode. For this reason, we test the effect of (1) spin, (2) mass, and (3) n_{ref} on the complex frequency of various GR and quantum modes in order to see the general differences between the two types of modes (see Figures 4-6 for frequency and Figures 7 for damping time). This is important to look at as these factors will influence the detectability of a mode, given that LIGO is most sensitive within a certain band (around 100 Hz, Figure 1).

We see that with increasing spin, the GR modes separate from each other, and increase in frequency. On the other hand, damping time for the modes does not really change with increasing spin. Increasing mass, for all modes (GR and quantum), decreases frequency and results in the two types of modes being closer together. For small n_{ref}, quantum modes are higher in frequency, but closer to GR modes (see Figures 4-6).

Compared to GR modes, the quantum mode tends to be longer lived; this tendency increases with mass, and higher refractive indices are overall longer-lived (see Figure 7). For instance, if we compare $n_{ref} = 3$ and $n_{ref} = 9$ for $M = 100M_\odot$ we see that for $n_{ref} = 3$ the damping time is around 0.01 seconds, but for $n_{ref} = 9$ the damping time is around 0.08 seconds. A long damping time *may* help recovery of the quantum mode. If, on one hand, the quantum mode dies off similar to the GR mode, it may be impossible to disentangle from higher order modes and the loud (2, 2) mode. But, if the quantum mode is long-lived, it will be present long after GR modes have died off.

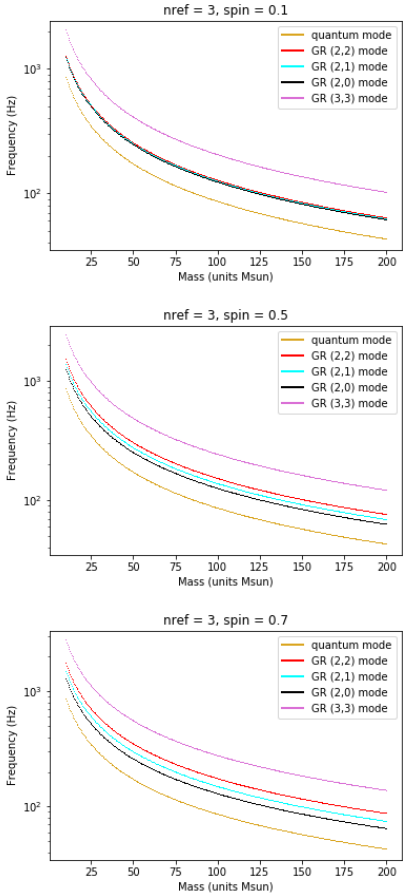

FIG. 4. Plot of frequency vs. mass (in units $M_\odot$) for GR modes (from (2,2) to (3,3)) and the quantum mode (yellow) for $n_{ref} = 3$. GR modes are calculated using `qnm` python package [19]. We see that with increasing spin, χ, the GR modes separate from one another and tend to increase in frequency. For higher mass values, the frequency of *all* modes decreases, as is clear by Equations 4 and 2. The quantum modes are lower in frequency than *all* the plotted GR modes, and the difference in frequency between GR modes and quantum modes decreases with increasing mass.

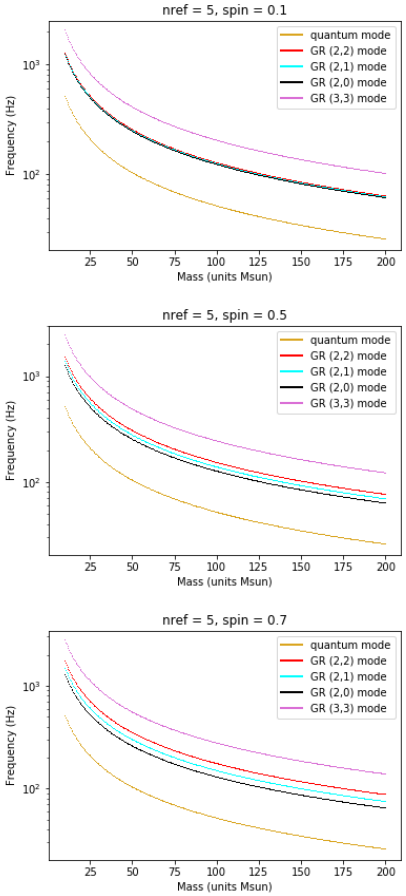

FIG. 5. Plot of frequency vs. mass (in units $M_\odot$) for GR modes (from (2,2) to (3,3)) and the quantum mode (yellow) for $n_{ref} = 5$. GR modes are calculated using `qnm` python package [19]. We see that with increasing spin, χ, the GR modes separate from one another and tend to increase in frequency. For higher mass values, the frequency of *all* modes decreases. The quantum modes are lower in frequency than *all* the plotted GR modes, and the difference in frequency between GR modes and quantum modes decreases with increasing mass.

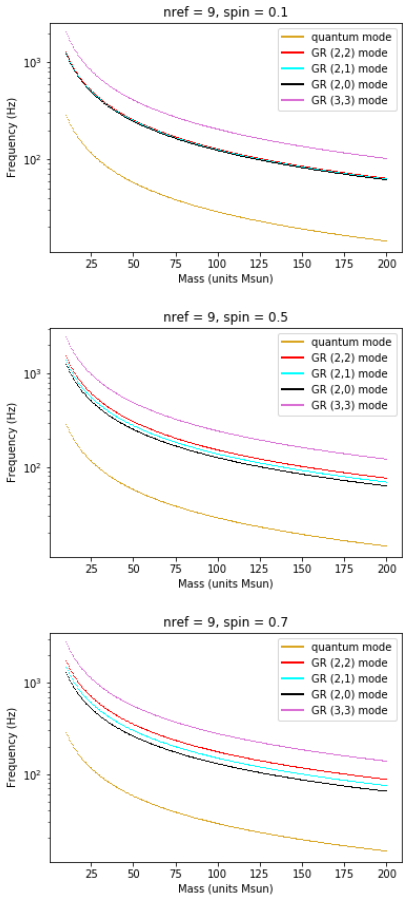

FIG. 6. Plot of frequency vs. mass (in units $M_\odot$) for GR modes (from (2,2) to (3,3)) and the quantum mode (yellow) for $n_{ref} = 9$. GR modes are calculated using `qnm` python package [19]. We see that with increasing spin, χ, the GR modes separate from one another and tend to increase in frequency. For higher mass values, the frequency of *all* modes decreases. The quantum modes are lower in frequency than *all* the plotted GR modes, and the difference in frequency between GR modes and quantum modes decreases with increasing mass.

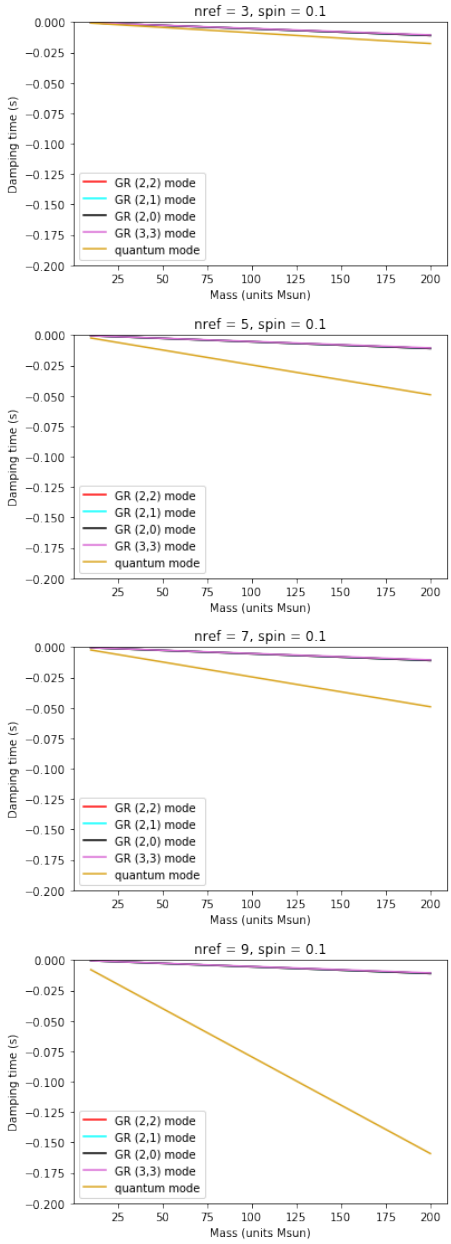

FIG. 7. Plot of damping time vs. mass (in units $M_\odot$) for GR modes (from (2,2) to (3,3)) and the quantum mode (yellow). We see that with increasing n_{ref}, damping time increases. Overall, the quantum mode is longer-lived than the GR mode.

C. Recovering Single Quantum Mode

Here, we explore under what circumstances is a *single* quantum mode best recovered: given an n_{ref}, what mass results in the highest Bayes factor? To do this, we inject our quantum mode into LIGO noise and recover using `bilby`; we repeat this process for a range of masses and n_{ref}. Below, we plot mass vs. the log Bayes factor for values of n_{ref} between 3 and 9. As a note, each point on the graph represents a single `bilby` run.

From Figures 8-11, we see that with increasing n_{ref}, the optimal detection range is shifted towards lower masses. For instance, for $n_{ref} = 3$ the peak mass is between 120-160$M_\odot$ while for $n_{ref} = 9$, the peak mass is between 40-60$M_\odot$. This is expected, as, increasing n_{ref} will result prohibitively low frequencies for high masses (Figure 4-6). In general, we see that loud signals (high SNR), tend to have the highest log (base 10) Bayes factor, which is unsurprising; a louder signal is more differentiable from the noise, thus more easily recovered.

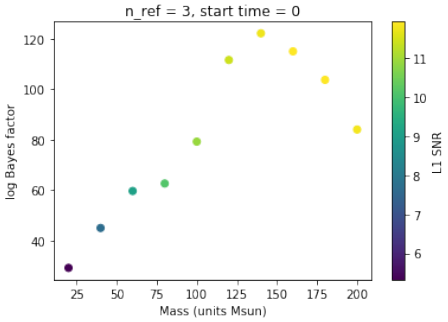

FIG. 8. For $n_{ref} = 3$ starting the waveform at $t_s = 0$, plot of mass (units $M_\odot$) vs. $\log_{10}$ Bayes factor, at a fixed amplitude 9×10^{-22}, resulting in a highest SNR of around 12 around the mass of $160M_\odot$.

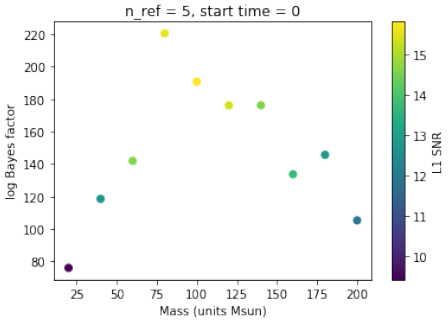

FIG. 9. For $n_{ref} = 5$ starting the waveform at $t_s = 0$, plot of mass (units $M_\odot$) vs. $\log_{10}$ Bayes factor, at a fixed amplitude 9×10^{-22}, resulting in a highest SNR of around 15 around the mass of $80M_\odot$.

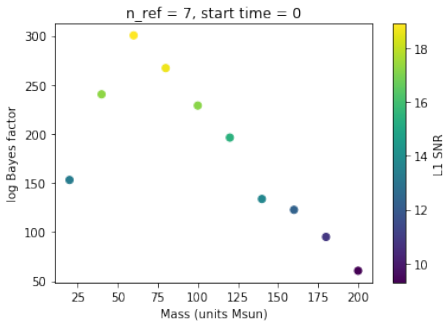

FIG. 10. For $n_{ref} = 7$ starting the waveform at $t_s = 0$, plot of mass (units $M_\odot$) vs. $\log_{10}$ Bayes factor, at a fixed amplitude 9×10^{-22}, resulting in a highest SNR of around 18 around the mass of $60M_\odot$.

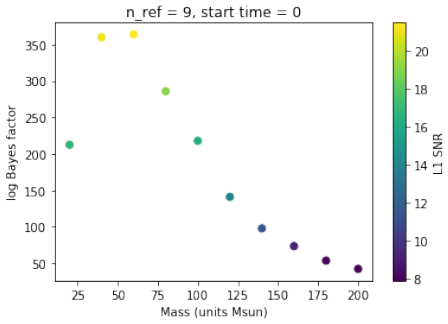

FIG. 11. For $n_{ref} = 9$ starting the waveform at $t_s = 0$, plot of mass (units $M_\odot$) vs. $\log_{10}$ Bayes factor, at a fixed amplitude 9×10^{-22}, resulting in a highest SNR of around 20 around the mass of $60M_\odot$.

Next, we look at whether parameters – the frequency and damping time of the quantum mode – can be recovered in `bilby`. We analyse the two extremes: $n_{ref} = 3$ and $n_{ref} = 9$ (see Figures 12-13). Looking at Figure 12 for $n_{ref} = 3$, we see that at both SNR = 4 and SNR = 9, the injected mode can be recovered, but the error on recovery is smaller with higher SNR. Similarly, looking at Figure 13 for $n_{ref} = 9$, we see that both SNR = 9 and SNR = 21 can recover injected mode within error, but that the error is smaller for higher SNR. In general, then, we see that we can recover *single* quantum modes in `bilby`, and that recovery fidelity increases with SNR.

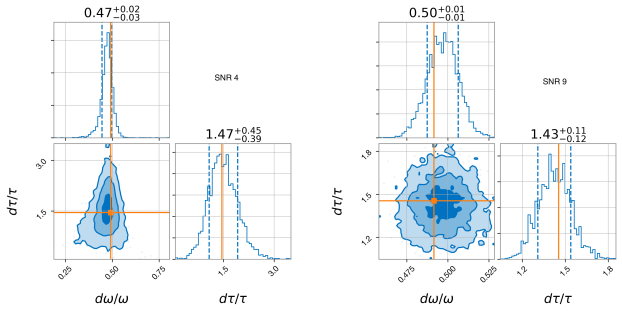

FIG. 12. Using $t_s = 0$, posterior distribution corner plots for $n_{ref} = 3$, $M = 140M_\odot$, and SNR 4 and 9 (as labeled). The input $\delta\omega/\omega = 0.49155$ while the input $\delta\tau/\tau = 1.45$ (again, these are in reference to the dominant (2, 2) mode). We see that, while our error bars sometimes do not include our inputted value, with increasing SNR, the peak is near the input (true) value, especially with regard to $\delta\tau/\tau = 1.45$.

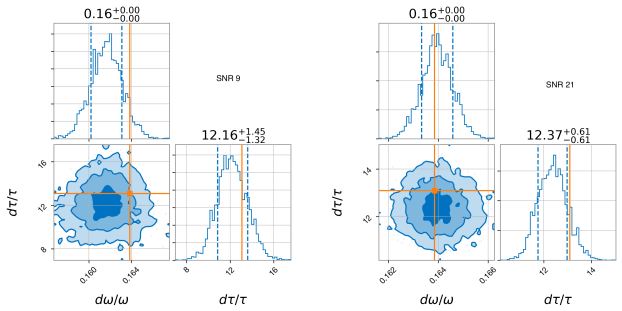

FIG. 13. Using $t_s = 0$, posterior distribution corner plots for $n_{ref} = 9$, $M = 60M_\odot$, and SNR 9 and 21 (as labeled). The input $\delta\omega/\omega = 0.16$ while the input $\delta\tau/\tau = 13.08$ (again, these are in reference to the dominant (2, 2) mode). We see that, while our error bars sometimes do not include our inputted value, with increasing SNR, the peak is near to input (true) value, especially with regard to $\delta\tau/\tau = 1.45$.

D. Recovering the Quantum Mode Within a Full Ringdown

Understanding the optimal masses for each n_{ref}, we move on to adding the quantum mode into a more realistic environment: the total GR ringdown including higher modes. We use NRSur7dq4 [18] to model the GR ringdown. Our goal is to (1) see whether the mode can be recovered within a full ringdown and (2) see what parameters (n_{ref} and corresponding peak mass) result in the *best* recovery. We use amplitude as a proxy for quantum signal SNR. We test between 6×10^{-23} to 6×10^{-22} for quantum signal amplitude; as a reference, the amplitude of the NRSur7dq4 signal (for masses between 50 and 100) tends to be around 1-3 orders greater. A very large quantum signal is unrealistic: if the phenomena we are exploring were loud, after all, they would have already been discovered in GW analyses (see Table III D for summary of all results).

For our priors, we only sample damping time (τ) and frequency (f_p), and set the priors for all other parameters to be their true values. The sampling prior on τ_p is log-uniform, and the sampling prior on f_p is uniform. So, as the signal becomes quieter (and recovery becomes harder), the posterior distribution on our sampled parameters will begin to look like the prior.

We see that with decreasing amplitude (and thus decreasing SNR) signal recovery becomes more difficult; parameter recovery fails for all n_{ref} at amplitude 8×10^{-23}. The question is what values of the parameters, specifically n_{ref} and corresponding peak mass, are better at parameter recovery (if at all).

Overall, we notice that n_{ref} between 5-9 evaluated at their corresponding peak mass are better recovered than lower and higher n_{ref} (they tend to have smaller bounds on error). Take for example, $n_{ref} = 3$ and $n_{ref} = 9$ at amplitude 2×10^{-22} (Figure 16). We see that parameter recovery fails totally for $n_{ref} = 3$ while it does not for $n_{ref} = 9$ (injected value is within error) (Figure 16). Furthermore, the posterior distributions of $n_{ref} = 3$ both τ_p and $f_{0,p}$ look like their priors.

This, for one, could be caused by higher n_{ref} values having longer damping times. If we look at the injected waveforms, for instance, for amplitude 6×10^{-22} (see Figure 15), the difference between the injected and original waveform is *most* visible for $n_{ref} = 9$. This is because the mode does not die off as quickly as smaller n_{ref}.

Nevertheless, $n_{ref} = 11$ evaluated at $M = 40$ has a long damping time but does not have as good parameter recovery. This is most likely because the GR frequency (the (2, 2) mode's frequency for this around 1000 Hz) is approaching to the detector's noisy band.

Really, what this suggests is n_{ref} around 5-9 recover parameters best. Based on work done in section C of the results – for recovery of a single quantum mode – this corresponds to a peak mass range between around $50M_\odot$ and $80M_\odot$. Again, as a reminder, peak mass corresponds to the mass at which a certain n_{ref} recovers parameters best.

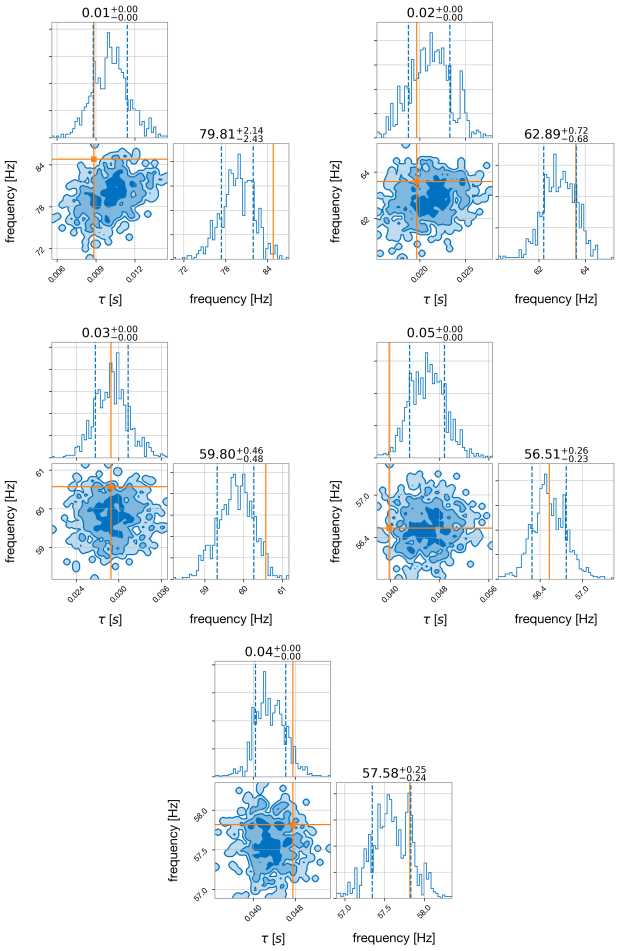

FIG. 14. Parameter recovery in `bilby` for amplitude 6×10^{-22} (units of strain) (see Figure 15 for plots of injection waveforms). The top left is $n_{ref} = 3$ for M=$100M_\odot$, the top right is $n_{ref} = 5$ for M=$80M_\odot$, the bottom left is $n_{ref} = 7$ for M=$60M_\odot$, the bottom right is $n_{ref} = 9$ for M=$50M_\odot$, and the bottom is $n_{ref} = 11$ for M=$40M_\odot$. Injected parameters are in orange. We see that with increasing n_{ref} parameter recovery improves, as the error bounds decrease. But, overall all n_{ref} can recover both τ_p and $f_{0,p}$.

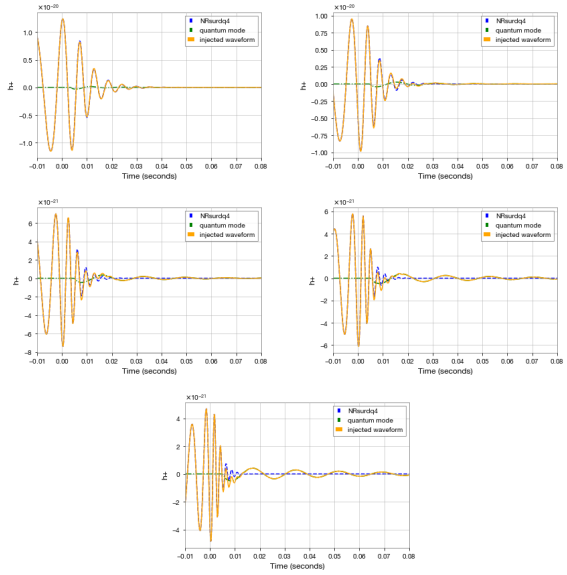

FIG. 15. Injected waveform with amplitude 6×10^{-22} where blue is the original (purely GR) NRSur7dq4, green is the additional quantum mode, and orange is the total injection waveform (NRSur7dq4 + quantum mode). The top left is $n_{ref} = 3$ for M = $100M_\odot$, the top right is $n_{ref} = 5$ for M = $80M_\odot$, the bottom left is $n_{ref} = 7$ for M = $60M_\odot$, the bottom right is $n_{ref} = 9$ for M = $50M_\odot$, and the bottom is $n_{ref} = 11$ for M = $40M_\odot$. We see that larger n_{ref} are longer lived.

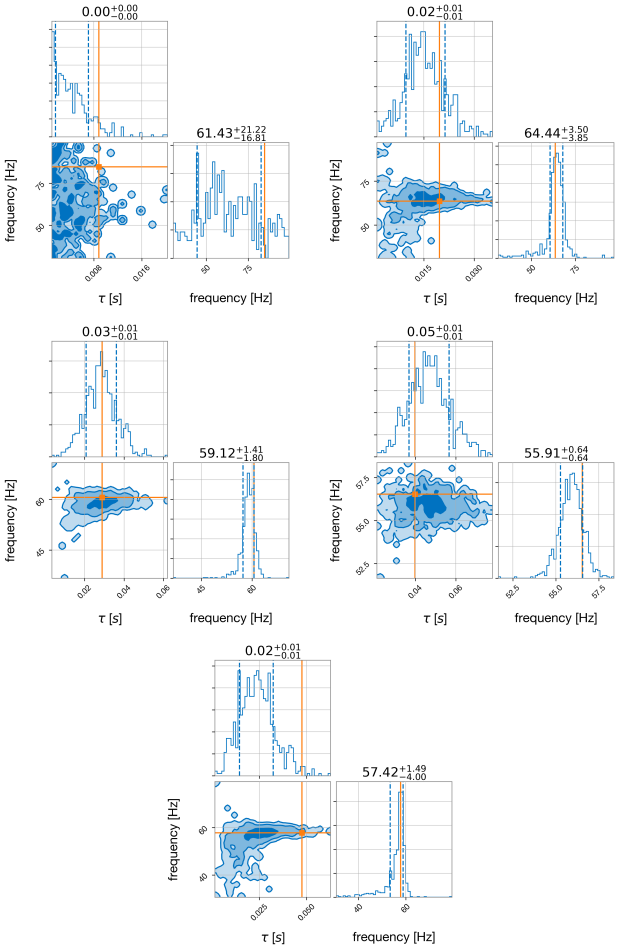

FIG. 16. Parameter recovery in `bilby` for amplitude 2×10^{-22} (units of strain) (see Figure 17 for plots of injection waveforms). The top left is $n_{ref} = 3$ for M = $100M_\odot$, the top right is $n_{ref} = 5$ for M = $80M_\odot$, the bottom left is $n_{ref} = 7$ for M = $60M_\odot$, the bottom right is $n_{ref} = 9$ for M = $50M_\odot$, and the bottom is $n_{ref} = 11$ for M = $40M_\odot$. $n_{ref} = 3$ (top left) is completely unable to recover the injected parameters; the posterior distribution on τ_p looks like the prior (log-uniform) and the posterior distribution on f_p looks like the its prior (uniform). On the other hand, $n_{ref} = 5$, $n_{ref} = 7$, $n_{ref} = 9$ all can, with $n_{ref} = 9$ marginally recovering parameters better (i.e. smaller error bounds). $n_{ref} = 5$, $n_{ref} = 7$, $n_{ref} = 9$, and $n_{ref} = 9$ do not look like their priors.

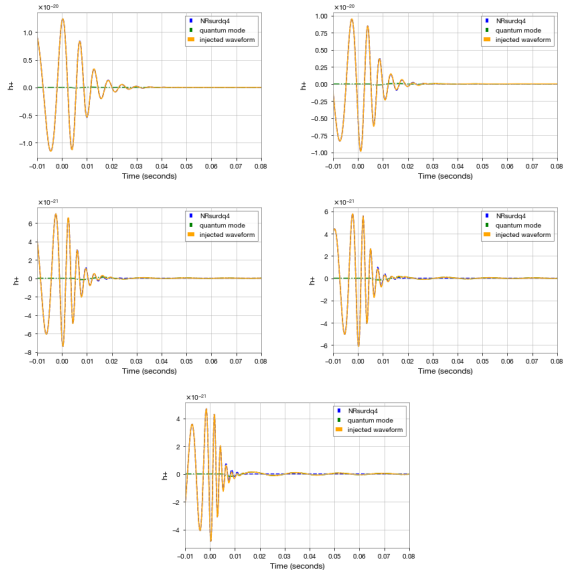

FIG. 17. Injected waveform with amplitude 2×10^{-22} where blue is the original (purely GR) NRSur7dq4, green is the additional quantum mode, and orange is the total injection waveform (NRSur7dq4 + quantum mode). The top left is $n_{ref} = 3$ for M = $100M_\odot$, the top right is $n_{ref} = 5$ for M = $80M_\odot$, the bottom left is $n_{ref} = 7$ for M = $60M_\odot$, and the bottom right is $n_{ref} = 9$ for M = $50M_\odot$. The difference between the original waveform (blue) and injected waveform (orange) is most noticeable in higher n_{ref}.

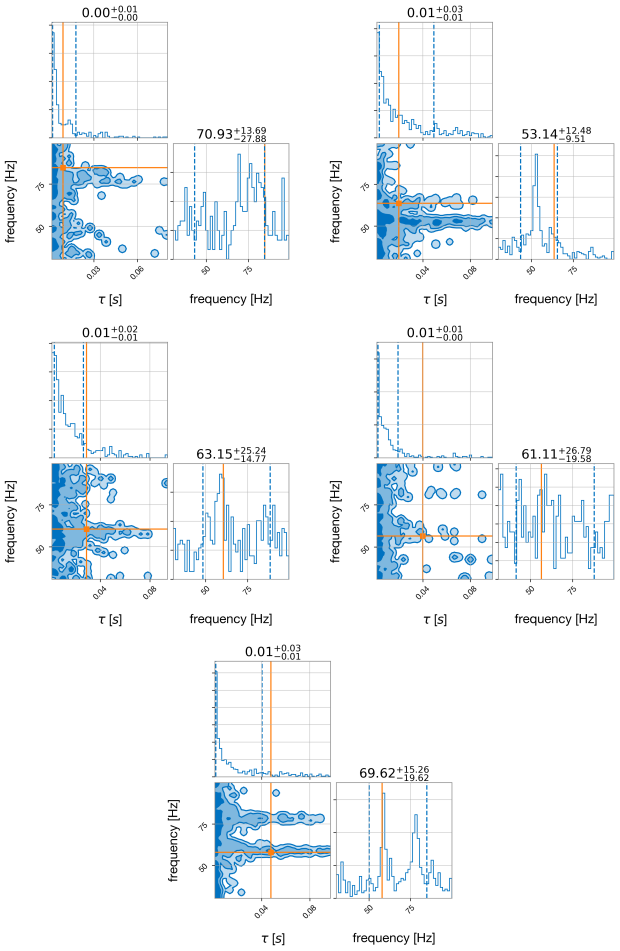

FIG. 18. Parameter recovery in `bilby` for Amplitude 8×10^{-23} (see Figure 19 for plots of injection waveforms). The top left is $n_{ref} = 3$ for M = $100M_\odot$, the top right is $n_{ref} = 5$ for M = $80M_\odot$, the bottom left is $n_{ref} = 7$ for M = $60M_\odot$, the bottom right is $n_{ref} = 9$ M = $50M_\odot$, and the bottom is $n_{ref} = 11$ for M = $40M_\odot$. Looking at the histograms, no n_{ref} is able to really recover well; all posteriors look like their priors (tau_p looks like a log-uniform distribution and $f_{0,p}$ looks like a uniform distribution.)

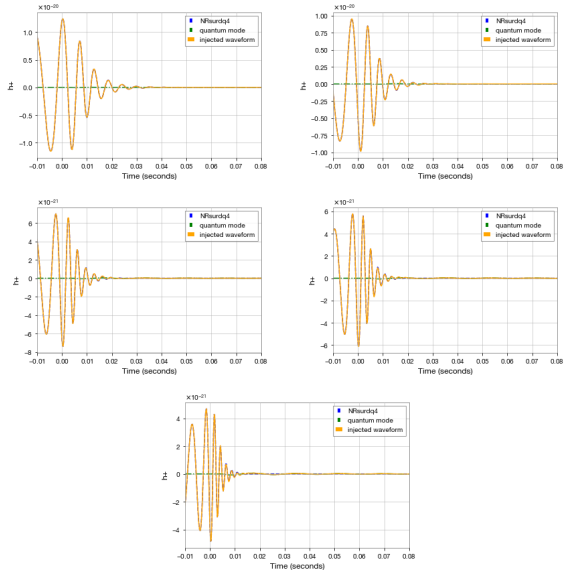

FIG. 19. Injected waveform with amplitude 8×10^{-23} where blue is the original (purely GR) NRSur7dq4, green is the additional quantum mode, and orange is the total injection waveform (NRSur7dq4 + quantum mode). The top left is $n_{ref} = 3$ for M = $100M_\odot$, the top right is $n_{ref} = 5$ for M = $80M_\odot$, the bottom left is $n_{ref} = 7$ for M = $60M_\odot$, the bottom right is $n_{ref} = 9$ for M = $50M_\odot$, and the bottom is $n_{ref} = 11$ for M = $40M_\odot$. Because of how small is amplitude is, there is no noticeable difference (by eye) between the the original waveform (blue) and the injected waveform (orange).

IV. CONCLUSIONS & FUTURE WORK

As gravitational wave detectors become more precise, multimodal observations – past the dominant (2, 2) mode – of BBH ringdown events will become a reality. The ringdown is where *small* deviations from GR may present themselves, be they quantum in nature or something completely unknown. The model explored in this paper by Brustein *et al* is one that models a black hole as non-empty (and non-classical) and filled with a stringy substance that has an index of refraction. This results in a new mode, distinct from GR modes, that is quantum in origin.

This mode is all around lower in frequency and longer-lived than GR modes, a tendency that increases with n_{ref}. What we find is that n_{ref} near 5-9 recover parameters best (τ_p and f_p). We also found that each n_{ref} performs best at a specific mass. The masses which perform best for n_{ref} between 5 and 9 are roughly 50-80$M_\odot$.

A next step will be to explore the parameter space more comprehensively. For one, we only considered inclination = 0 systems and equal mass mergers (q = 1). Inclination influences the proportion of higher order modes. Including non-equal mass mergers may make recovery harder; higher q mergers have relatively stronger higher order modes. We must also consider whether using a more complicated model (i.e. NRSur7dq4 + quantum mode) *actually* has more evidence for it than the simpler GR model. To do this, we will use model selection with the Bayesian Odds ratio. This is important for quantifying the statistical significance of detection. As detectors become more sensitive in the coming years, it will become possible to look into the ringdown spectrum and see possible deviations from GR. What is important, however, is that these deviations are statistically *significant* and not just the result of noise.

V. ACKNOWLEDGMENTS

I'd like to thank my mentors, Dr. Alan J. Weinstein and Dr. Colm Talbot for all their help diving into gravitational wave science. I'd also like to thank Jen, Erin, Darin, and the Astrophysics group for their continuous support. Finally, I'd like to thank the NSF REU program, Caltech LIGO SURF program, and the Caltech SURF program for providing this opportunity.

[1] T. Moore, *A General Relativity Workbook* (University Science Books, 2012).
[2] J. Aasi, B. P. Abbott, R. Abbott, T. Abbott, M. R. Abernathy, K. Ackley, C. Adams, T. Adams, P. Addesso, and et al., Advanced ligo, Classical and Quantum Gravity **32**, 074001 (2015).
[3] F. Acernese, M. Agathos, K. Agatsuma, D. Aisa, N. Allemandou, A. Allocca, J. Amarni, P. Astone, G. Balestri, G. Ballardin, and et al., Advanced virgo: a second-generation interferometric gravitational wave detector, Classical and Quantum Gravity **32**, 024001 (2014).
[4] B. Abbott, R. Abbott, T. Abbott, M. Abernathy, F. Acernese, K. Ackley, C. Adams, T. Adams, P. Addesso, R. Adhikari, and et al., Observation of gravitational waves from a binary black hole merger, Physical Review Letters **116**, 10.1103/physrevlett.116.061102 (2016).
[5] E. Berti, V. Cardoso, and A. O. Starinets, Quasinormal modes of black holes and black branes, Classical and Quantum Gravity **26**, 163001 (2009).
[6] R. Abbott, T. Abbott, S. Abraham, F. Acernese, K. Ackley, C. Adams, R. Adhikari, V. Adya, C. Affeldt, M. Agathos, and et al., Gw190412: Observation of a binary-black-hole coalescence with asymmetric masses, Physical Review D **102**, 10.1103/physrevd.102.043015 (2020).
[7] R. A. Konoplya and A. Zhidenko, Quasinormal modes of black holes: From astrophysics to string theory, Reviews of Modern Physics **83**, 793–836 (2011).
[8] B. Abbott, R. Abbott, T. Abbott, S. Abraham, F. Acernese, K. Ackley, C. Adams, R. Adhikari, V. Adya, C. Affeldt, and et al., Gwtc-1: A gravitational-wave transient catalog of compact binary mergers observed by ligo and virgo during the first and second observing runs, Physical Review X **9**, 10.1103/physrevx.9.031040 (2019).
[9] Lorentzian function: Wolfram mathworld, `https://mathworld.wolfram.com/LorentzianFunction.html`.
[10] R. Abbott, T. D. Abbott, S. Abraham, F. Acernese, K. Ackley, C. Adams, R. X. Adhikari, V. B. Adya, C. Affeldt, M. Agathos, and et al., Gw190814: Gravitational waves from the coalescence of a 23 solar mass black hole with a 2.6 solar mass compact object, The Astrophysical Journal **896**, L44 (2020).
[11] R. Brustein and A. Medved, Non-singular black holes interiors need physics beyond the standard model, Fortschritte der Physik **67**, 1900058 (2019).
[12] R. Brustein and Y. Sherf, Emission channels from perturbed quantum black holes, Phys. Rev. D **100**, 124005 (2019).
[13] R. Brustein, A. Medved, and K. Yagi, When black holes collide: Probing the interior composition by the spectrum of ringdown modes and emitted gravitational waves, Physical Review D **96**, 10.1103/physrevd.96.064033 (2017).
[14] A. Z. . D. Robbins, *String Theory for Dummies* (Wiley Publishing, 2010).
[15] Scipy docs, `https://docs.scipy.org/doc/scipy/reference/tutorial/optimize.html`.
[16] Bilby documentation, `https://lscsoft.docs.ligo.org/bilby/index.html`.
[17] G. Ashton, M. Hübner, P. D. Lasky, C. Talbot, K. Ackley, S. Biscoveanu, Q. Chu, A. Divakarla, P. J. Easter, B. Goncharov, and et al., Bilby: A user-friendly bayesian inference library for gravitational-wave astronomy, The Astrophysical Journal Supplement Series **241**, 27 (2019).
[18] S. E. Field, C. R. Galley, J. S. Hesthaven, J. Kaye, and M. Tiglio, Fast prediction and evaluation of gravitational

waveforms using surrogate models, Physical Review X **4**, 10.1103/physrevx.4.031006 (2014).
[19] `qnm` documentation, `https://qnm.readthedocs.io/en/latest/`.

TABLE I. Summary table for all `bilby` in section D of Results. Here, A_p is the amplitude of the injected quantum mode, mass is the peak mass (in units $M_\odot$) for the run's n_{ref} value. The recovered parameters are frequency of the quantum mode ($f_{0,p}$) and damping time of the quantum mode (τ_p).

A_p (units strain)	Mass ($M_\odot$)	n_{ref}	injected $f_{0,p}$ (Hz)	injected τ_p (s)	recovered $f_{0,p}$ (Hz)	recovered τ_p (s)
2×10^{-22}	$100M_\odot$	3	84.79 Hz	0.009 s	79.81 Hz (+ 2.14, - 2.43)	0.01 s ($+ 5\times10^{-5}, -5 \times 10^{-5}$)
2×10^{-22}	$80M_\odot$	5	63.59 Hz	0.009 s	61.43 Hz (+ 21.22, - 16.81)	0.004 s (+ 0.002, - 0.002)
2×10^{-22}	$60M_\odot$	7	60.57 Hz	0.029 s	59.12 Hz (+ 1.41, - 1.80)	0.03 s (+ 0.01, - 0.01)
2×10^{-22}	$50M_\odot$	9	56.53 Hz	0.040 s	55.19 Hz (+ 0.64, - 0.64)	0.05 s (+ 0.01, - 0.01)
2×10^{-22}	$40M_\odot$	11	57.81 Hz	0.048 s	57.42 Hz (+ 1.49, - 4.00)	0.02 s (+ 0.01, - 0.01)
2×10^{-22}	$100M_\odot$	3	84.79 Hz	0.009 s	79.81 Hz (+ 2.14, - 2.43)	0.01 ($+ 5\times10^{-5}, -5 \times 10^{-5}$)
2×10^{-22}	$80M_\odot$	5	63.59 Hz	0.009 s	61.43 Hz (+ 21.22, - 16.81)	0.004 s (+ 0.002, - 0.002)
2×10^{-22}	$60M_\odot$	7	60.57 Hz	0.029 s	59.12 Hz (+ 1.41, - 1.80)	0.03 s (+ 0.01, - 0.01)
2×10^{-22}	$50M_\odot$	9	56.53 Hz	0.040 s	55.19 Hz (+ 0.64, - 0.64)	0.05 s (+ 0.01, - 0.01)
2×10^{-22}	$40M_\odot$	11	57.81 Hz	0.048 s	57.42 Hz (+ 1.49, - 4.00)	0.02 s (+ 0.01, - 0.01)
8×10^{-23}	$100M_\odot$	3	84.79 Hz	0.009 s	79.81 Hz (+ 2.14, - 2.43)	0.00 s (+ 0.01, - 0)
8×10^{-23}	$80M_\odot$	5	63.59 Hz	0.009 s	53.14 Hz (+ 12.48, - 9.51)	0.01 s (+ 0.03, - 0.01)
8×10^{-23}	$60M_\odot$	7	60.57 Hz	0.029 s	63.15 Hz (+ 25.24, - 14.77)	0.01 s (+ 0.02, - 0.01)
8×10^{-23}	$50M_\odot$	9	56.53 Hz	0.040 s	61.11 Hz (+ 26.79, - 19.58)	0.01 s (+ 0.01, - 0)
8×10^{-23}	$40M_\odot$	11	57.81 Hz	0.048 s	69.62 Hz (+ 12.26, - 19.62)	0.01 s (+ 0.03, - 0.01)